On the use of superparamagnetic hydroxyapatite nanoparticles as agent for magnetic and nuclear in vivo imaging

Alessio Adamiano[a], Michele Iafisco[a], Monica Sandri[a], Martina Basini[b], Paolo Arosio[b], Tamara Canu[c], Giovanni Sitia[d], Vincenzo Iannotti[e], Giovanni Ausanio[e], Antonio Esposito[c,f,g], Eirini Fragogeorgi[h], Maritina Rouchota[i], George Loudos[h,i], Alessandro Lascialfari[b,j] and Anna Tampieri[a]

[a] *Institute of Science and Technology for Ceramics (ISTEC), National Research Council (CNR), Via Granarolo 64, 48018 Faenza, Italy*

[b] *Physics Department and INSTM, Università degli Studi di Milano, Via Celoria 16, 20133 Milano, Italy*

[c] *Preclinical Imaging Facility Experimental Imaging Centre, IRCCS San Raffaele Scientific Institute and Università Vita-Salute San Raffaele, Via Olgettina 58, 20132 Milano, Italy*

[d] *Experimental Hepatology Unit, Division of Immunology, Transplantation and Infectious Diseases, IRCCS San Raffaele Scientific Institute, Via Olgettina 58, 20132 Milano, Italy*

[e] *CNR-SPIN and Department of Physics "E. Pancini", University of Naples "Federico II", Piazzale V. Tecchio 80, I-80125 Napoli, Italy*

[f] *Vita-Salute San Raffaele University, Via Olgettina 58, 20132 Milan, Italy*

[g] *Department of Radiology, IRCCS San Raffaele Scientific Institute, Milan, Italy,*
[h] *Institute of Nuclear & Radiological Sciences, Technology, Energy & Safety, NCSR "Demokritos", Greece.*

[i] *Bioemission Technology Solutions, Alexandras 116, Athens, Greece*

[j] *Istituto di Nano scienze, CNR-S3, Via Campi 213/A, 41125 Modena, Italy*

Author for correspondence: Dr. Alessio Adamiano

Institute of Science and Technology for Ceramics (ISTEC) National Research Council (CNR),

Via Granarolo 64, 48018 Faenza (RA), Italy.

E-mail: alessio.adamiano@istec.cnr.it

Tel: +39 0546699761

Abstract

Superparamagnetic iron oxide nanoparticles (NPs) are the most employed magnetic nanomaterials for advanced clinical applications such as drug carriers and multimodal imaging agents. Due to raising concerns about iron accumulation in soft issues associated to their administration, the identification of alternative biocompatible magnetic NPs is an important need. Here, we report on the performance of previously synthetized superparamagnetic iron-doped hydroxyapatite (FeHA) NPs as contrast agent for magnetic resonance (MRI). The contrast abilities of FeHA and Endorem® - which was here used as reference material - were assessed by ^{1}H nuclear magnetic resonance relaxometry showing that the transversal relaxivity of FeHA was higher with respect to that of Endorem® at clinical magnetic field of 1.5 Tesla (165 s^{-1} mM^{-1} vs 103 s^{-1} mM^{-1}). Their performance in healthy mice at low iron dose (1 mg kg^{-1}) was monitored by a 7 Tesla MRI scanner, revealing that FeHA applied a higher contrast enhancement, and had a longer endurance in the liver with respect to Endorem® at iron equality. The proof of concept for FeHA to act as single photon emission computed tomography (SPECT) and positron emission tomography (PET) imaging agent was also provided highlighting its potential use as dual modality SPECT/PET-MRI contrast agent. FeHA NPs were successfully surface labeled with 99m-technetium-methylene diphosphonate (^{99m}Tc-MDP) employing a straightforward one-pot procedure and their *in vivo* imaging ability was proved. *In vivo* scintigraphy/x-ray fused imaging and *ex vivo* studies confirmed FeHA dominant accumulation in the liver, and secondarily in other organs containing cells of the mononuclear phagocyte system as detected by MRI. FeHA efficiency as MRI-T_2 and SPECT/PET imaging agent combined to its intrinsic biocompatibility qualify it as a valid alternative to the currently used magnetic NPs for interesting medical applications.

1.Introduction

Magnetic nanoparticles (MNPs) have received much attention in the last decade due to their suitability for a wide variety of functions, going from magnetic recording to intriguing therapeutic and diagnostic medical applications [1-4].

Due to their inherent low toxicity [5, 6] and relative ease of synthesis [7] superparamagnetic iron oxide nanoparticles (SPIONs) are the most studied MNPs for clinical applications, mainly as MRI contrast agent (CA). Some of them, such as dextran and carboxydextran coated Ferumoxide and Ferucarbotran were approved for clinical use by FDA in the ’90 as CA for the liver. However clinical concerns associated with their use are emerging. These latter rely on the presence of high concentration of iron-rich MNPs in a localized area that, on the other hand, is necessary to maximize the diagnostic function, as on the *in vivo* durability of the coating whose function goes from preventing the release of iron ions to conferring biocompatibility and colloidal stability to the SPIONs [8-11]. The coatings instability and the high concentration of SPIONs in the therapeutic site can result in a high biological risk caused by the latent exposition of tissues/organs to an overload of iron potentially triggering cytotoxicity, DNA damage, inflammatory events and many other adverse effects [12]. More specifically, high levels of iron excess deriving from SPIONs administration have been persistently observed in liver tissues over weeks in cirrhotic patients in the need of reliable MRI diagnosis [13]. These facts highlight the importance of developing novel biocompatible MNPs based CA containing low amount of iron and having the same efficiency of SPIONs in term of contrast enhancement [14].

Synthetic hydroxyapatite (HA) is the most widely used bioceramic for the repair and regeneration of bone tissue defects [15]. The recent progresses in the preparation of nano-sized HA with tailored surface characteristics, and colloidal stability as well as their intrinsically biocompatibility, biodegradability and non-immunogenicity have opened new perspectives in their use for applications not related to bone [16, 17]. In this domain, HA nanoparticles (NPs) have been proposed in a wide variety of nanomedical applications spanning from diagnosis to therapy [16, 18-20].

HA presents a highly flexible structure that can easily incorporate foreign ions inducing modifications in its physico-chemical properties. It was reported that HA NPs can be endowed with a range of abilities not displayed by mere HA, such as photocatalytic, luminescent and magnetic properties, by doping with Ti, Eu and Fe respectively [21-23]. Employing this strategy, in our previous works, we reported on the synthesis and applications (i.e. as anticancer drug carriers and magnetic label of stem cells) of iron doped HA NPs (FeHA) of 10–30 nm in width and 70–100 nm in length, displaying a superparamagnetic behavior and no residual magnetization at room temperature, reaching a specific magnetization at saturation (M_s) of 8.9 emu g^{-1} [23, 24].

Here we sought to assess whether FeHA, due to their superparamagnetic features and favorable biocompatibility can be suitable as MRI CA. The use of ion doped HA as MRI CA is not new, and Gd^{3+}, Dy^{3+}, Fe^{3+} doped HA were already proposed for this application [18, 25, 26]. In this respect, it is important to remark that NPs doped with lanthanide ions feature a paramagnetic behavior, thus limiting their utilization as multifunctional or "theranostic" nanomaterial able to combine diagnosis and therapy that are nowadays at forefront of nanomedicine research. In fact the superparamagnetism is a requirement of MNPs to accomplish the most promising therapeutic applications such as hyperthermia, magnetofection, cell magnetization for stem-cell therapy and drug nano-carries [1, 27-29].

In the present study, the MRI performance of FeHA was tested *in vitro* and *in vivo* on mice evaluating the negative T_2 contrast enhancement achieved in the liver. FeHA performances were compared to those obtained using FDA-approved SPION's based CA (i.e. Endorem®), which was already used in clinical trials for the diagnosis of hepatic metastases [30-32]. SPIONs based CAs are rapidly incorporated by Kupffer cells of the liver and by cells of the mononuclear phagocyte system (MPS) located in other organs. In this work, the degradation/clearance of FeHA and Endorem from the liver, spleen and kidneys of treated mice has been monitored by the loss of the T_2 contrast enhancement over time [33]. The follow-up was extended up to the clearance of MNPs that was considered completed when T_2 signals reached pre-injection (basal) values.

The synergistic combination of MRI with single photon emission computed tomography (SPECT) and /or positron emission tomography (PET) is likely to become the next generation of dual-modality scanners in medical imaging [34, 35]. These instruments will provide patients with accurate diagnoses thanks to the sensitive and quantifiable signal of SPECT/PET and the high soft-tissue resolution of MRI [36]. As a consequence, there has been an increasing interest in the development of dual-modality SPECT/PET–MRI contrast agents.

Due to the presence of coatings, to date the radiolabeling of SPIONs has been achieved only by complicated chemical conjugation strategies or after thermal treatments [37]. The trade-off between additional functionality and complexity is the subject of ongoing debate, however it is undisputable that supplementary synthetic steps means extra costs, more convoluted behavior and effects in vivo, and also greater regulatory hurdles to be overcome [38]. Here the feasibility to radiolabel FeHA NPs with 99m-technetium-methylene diphosphonate (^{99m}Tc-MDP) employing a straightforward and reproducible procedure as well as their *in vivo* imaging ability was proved.

This work mainly demonstrates the potential of FeHA NPs for the development of targeted multimodal SPECT/PET-MRI imaging agents.

2. Materials

2.1 FeHA synthesis

FeHA was synthesised according to the method reported by Adamiano et *al.* [24] with some minor modifications. Briefly, a solution obtained by mixing 8.87 g of H_3PO_4 (85 wt% Merck) with 30 mL of deionized water was added drop-wise into a $Ca(OH)_2$ suspension added with $FeCl_2$ and $FeCl_3$ in a 1:1 ratio at 45°C under vigorous stirring. When the neutralization reaction was completed, the growth solution was kept at 45 °C under constant stirring at 400 rpm for 3 hours and left still at room temperature overnight. FeHA was then recovered by centrifugation of the reaction mixture to be repeatedly rinsed with water and finally re-suspended in a citrate buffer 0.1 wt% for MRI experiment, while an aliquot was freeze-dried, ground in a mortar and sieved using a 150 μm mesh filter for physico-chemical characterizations.

Endorem® (Guerbet, France) was used as a reference material for comparison with FeHA, and consists of a water suspension of 15.6 mg mL^{-1} of magnetite and maghemite NPs coated by dextran (Ferumoxides).

2.2 Samples Characterization

The chemical composition of FeHA and Endorem® was determined dissolving an aliquot of sample in a diluted HNO_3 solution (~ 2 wt%) and in a 1:3 HNO_3:HCl solution, respectively. The obtained solutions were analyzed by an inductively coupled plasma spectrometer (ICP-OES) (Liberty 200, Varian, US) employing wavelengths of 422.673 nm (Ca), 259.940 nm (Fe), and 213.618 nm (P). The values shown in this study are an average of three replicates, and are reported in terms of Fe, Ca, P and carbonate wt%, and (Fe + Ca)/P and Ca/P molar ratios.

The carbonate content in FeHA was evaluated on dried samples by thermogravimetric analysis (TGA) investigations using a Stanton STA 1500 (Stanton, London, UK) apparatus. About 10 mg of powder was weighed in a platinum crucible and heated from room temperature to 1100 °C under nitrogen flow. The heating rate was 10 °C min^{-1} and alumina was used as reference standard. The CO_3^{2-} content was evaluated according to the weight loss observed between 550 and 950 °C as already described in the literature for carbonated HA [39, 40].

FeHA crystal structure was analyzed by a D8 Advance Diffractometer (Bruker, Karlsruhe, Germany) equipped with a Lynx-eye position sensitive detector using Cu Kα radiation (λ = 1.54178 Å) generated at 40 kV and 40 mA, operating in the 2θ range between 10° and 80° with a step size (2θ) of 0.02° and a counting time of 0.5 s. Quantitative evaluation of phase compositions and cell parameters was performed by full-profile Rietveld analysis of the XRD spectrum (TOPAS v. 4.2, Bruker AXS, Karlsruhe, Germany).

ζ-potential distributions of FeHA and Endorem® NPs were measured by dynamic light scattering (DLS) with a Zetasizer Nano ZS (Malvern Ltd., Worcestershire, UK) and were quantified by laser Doppler velocimetry as electrophoretic mobility using disposable electrophoretic cell (DTS1061, Malvern Ltd., Worcestershire, UK). The measurements were carried out suspending the NPs in an HEPES buffer 0.01M at pH= 7.4. Ten runs of 30 s were performed for each measurement and four measurements were carried out for each sample. The same conditions and the same buffer were used to measure the zeta average values and the hydrodynamic diameter distributions of both Endorem® and FeHA.

Samples morphology and size in dry state were analyzed with a FEI Tecnai F20 transmission electron microscopy (TEM) equipped with a Schottky emitter and operating at 120 and 200 keV. 10 μL of FeHA suspended in citrate buffer 0.1 wt% at 12.5 mg mL^{-1} were dissolved in 5 mL of isopropanol and treated with ultrasound, while in the case of Endorem® the same procedure was followed using a stock solution containing 15.8 mg mL^{-1} of iron oxide NPs. A droplet of the resulting finely dispersed suspensions was evaporated at room temperature and under atmospheric pressure on a holey carbon film.

2.3 Nuclear Magnetic Resonance and Magnetic Characterization

The spin dynamics and in particular the MRI contrast efficiency was assessed by means of 1H nuclear magnetic resonance (1H-NMR) relaxometry characterization. The NMR-dispersion profile was performed at room temperature by measuring the longitudinal and the transverse nuclear relaxation times T1 and T2 in the frequency range $10\ kHz \leq \nu \leq 170\ MHz$, on FeHA and Endorem® NPs dispersed in a citrate buffer 0.1 wt% at pH=6.0 and at Fe concentration of 0.2 mM.

The NMR signal detection and generation was obtained by a Smartracer Stelar relaxometer (for $10\ kHz \leq \nu \leq 9.5\ MHz$) which makes use of the fast-field-cycling technique and a Stelar Spinmaster and an Apollo-Tecmag Fourier transform-nuclear magnetic resonance (FT-NMR) spectrometer (for $\nu \geq 9.5\ MHz$). FeHA Ms was measured from its magnetic hysteresis loop collected with a vibrating sample magnetometer (VSM, Oxford 203 Instruments, Maglab 9T), operating at a vibration frequency of 55 Hz, in the maximum applied magnetic field H_{max} = 50 KOe at 300 K. Before carrying out any type of measurement, the specimen was accurately demagnetized.

2.4 MRI experiments

A screening of FeHA and Endorem® contrast abilities in aqueous solution was conducted at five different iron concentrations from 0.002 mM to 0.15 mM to identify the optimal conditions for the *in vivo* experiments, similarly to what is already reported in the literature about liver MRI imaging with

SPIONs [8]. A preliminary *in-vitro* experiment was conducted on a 7 Tesla MRI scanner (Bruker, BioSpec 70/30 USR, Paravision 5.1), equipped with 450/675 mT m^{-1} gradients (slew-rate: 3400-4500 T/m/s; rise-time 140 μs) and a circular polarized mouse body volume coil with an inner diameter of 40 mm, using a multi-slice multi-echo (MSME) sequence with the following parameters: Repetition time (TR)= 2500 ms, 16 echos registered separately with first echo time (TE1)= 10.73 ms and echo spacing =10.73 ms, field of view (FOV) = 20 mm x 40 mm, spatial resolution = 0.078 x 0.208 mm $pixel^{-1}$, scan time = 8 min.

In-vivo experiments were performed using the same 7 Tesla MRI scanner and coil. During MRI experiments all mice were maintained under general anaesthesia by 1.5 – 2% isoflurane vaporized in 100% oxygen (flow: 1 L min^{-1}). Breathing and body temperature were monitored during MRI (SA Instruments, Inc., Stony Brook, NY, USA) and maintained around 30 breaths-per-minute and 37°C, respectively

MR images were collected using MSME, fast low-angle shot gradient echo sequence (2D-FLASH) and Rapid Acquisition with Relaxation Enhancement (RARE) T2-weighted sequences. All the sequences were acquired with the same field of view (FOV = 34 mmx18 mm) and thickness (1mm). Imaging parameters for MSME were as follows: Repetition time (TR)= 2500 ms, 12 echos registered separately with first echo time (TE1)= 8.79 ms and echo spacing =8.79 ms, spatial resolution = 0.177 x 0.180 mm/pixel, scan time = 6 min, 18 slices.

Imaging parameters for 2D-FLASH were as follows: TR = 450 ms, TE = 3.25 ms, Flip Angle =30°, spatial resolution = 0.133 x 0.094 mm $pixel^{-1}$, scan time = 2 min, 24 slices.

Imaging parameters for RARE T2 were as follows: TR = 3500 ms, TE =30 ms, spatial resolution = 0.133 x 0.08 mm $pixel^{-1}$, scan time = 2 min, 24 slices.

For the *in vivo* experiments, C57BL/6 healthy male mice were divided in two groups and injected intravenously with two solution of FeHA and Endorem® NPs at 0.05 mM of Fe in a 5 wt% glucose solution so to obtain an equivalent dose of 1 mg kg^{-1} of iron per mouse. More in detail, the first group of mice was treated with a dose of 10.3 mg kg^{-1} of FeHA (9.7 wt% of Fe, data from ICP), while the second group was treated with a dose of 1.43 mg kg^{-1} of Endorem®.

MR images of the mice liver were collected at the following time points: pre-injection, and then post-injection at 10 minutes and 24 hours. The signal intensities were measured from a region of interest (ROI) of 0.10 cm^2 for the liver, 0.07 cm^2 for the spleen and 0.17 cm^2 for the renal cortex.

MR images of the mice treated with FeHA were collected daily for ten consecutive days to follow the clearance of NPs from the liver, the spleen and the renal cortex. All mice were maintained in microinsulator cages under a 12-hour light/12-hour dark cycle with free access to water and standard mouse diet (Teklad Global 18% Protein Rodent Diet, Harlan) within the Experimental Imaging

Center O (CIS) facility at the San Raffaele Scientific Institute. All procedures on mice were approved by the San Raffaele Institutional Animal Care and Use Committee (IACUC 691) according to institutional guidelines in compliance with national (D.L. N.26, 04/03/2014) and international law and policies (new directive 2010/63/EU). Special attention was paid to animal welfare and to minimize the number of animals used and their suffering.

2.5 Radiolabeling of FeHA

For FeHA radiolabeling, the short-lived and single photon γ-emitting metastable isotope of technetium, Tc (^{99m}Tc) was used. In brief, fresh $Na^{99m}TcO_4$ generator (DrytecTM, GE Healthcare (US)) eluate (~10–20 mCi) was added to the MDP kit (PoltechMDP, 5mg, Polatom (PL)). Next, ^{99m}Tc-MDP conjugate was left for 10 min and its labelling efficiency was confirmed by chromatography analysis with silica gel paper chromatography (ITLC-SG) using methyl-ethyl-ketone and 136 g L^{-1} sodium acetate as the mobile phases. An aliquot of 100 μL of ^{99m}Tc-MDP were added to 900 μL FeHA suspension (5 mg ml^{-1}) and the mixture was allowed to react at room temperature under constant stirring for 30 min. FeHA suspensions were then centrifuged twice for 15 min (14.000 rpm) at 4 °C and the radioactivity in the pellet and the supernatant were measured by an Atomlab 100 Dose Calibrator (Biodex Medical Systems Inc.) to provide the percentage of radioactivity of the NPs. Quality control of the re-suspended pellet of ^{99m}Tc-MDP-FeHA was done with paper chromatography Whatman 3MM (GE Healthcare (UK)) using saline buffer (NaCl 0.9 wt%) as the mobile phase. ITLC analysis was performed on a Scan-RAM radio TLC detector (LabLogic Systems Ltd., (UK)). The chemicals and reagents used were of analytical grade.

2.6 Stability study of radiolabeled FeHA

In vitro stability assay was performed, at 0 min, 1 h, 3 h and 24 h post-conjugation, over a range of temperatures (at 5 °C, 25 °C and 37 °C) and in different media namely isotonic saline solution, human and bovine fetal serums at 37 °C. The time-dependent increase of any free radioligand of ^{99m}Tc-MDP was determined by using saline as the mobile phase system in Whatman 3MM or ITLC-SG strip.

2.7 Biodistribution and whole body scintigraphy/x-ray fused imaging of radiolabeled FeHA in healthy mice

In vivo studies were performed at the NCSR Demokritos (Aghia-Paraskevi, Attica Prefecture, Greece), using female normal Swiss-Webster Albino mice (15-25g) purchased from the Breeding Facilities of the NCSR Demokritos (Permit Number: EL 25 BIO 019, EL 25 BIO 020). The protocol and all the animal procedures were approved by the General Directorate of Veterinary Services

(Athens, Attica Prefecture, Greece) and by the Bioethical Committee of the Institution (Permit number: EL 25 BIO 022) on the basis of the European Directive 2010/63/EU on the protection of animals used for experimental purposes.

The *ex vivo* profile in healthy mice was studied by injecting 100 μL, ~0.1 mCi (3.7 MBq) corresponding to ~400 μg of the radiolabeled FeHA (0.3 mg Fe per body mouse) in saline solution (pH: 7.0), via the tail vein. Animals were sacrificed at pre-determined time intervals of 30 min, 40 min, 4h and 24 h post injection and the main organs or tissues were removed, weighed and counted, together with blood samples, muscle and urine, by a γ-counter system (Cobra II from Packard, Canberra). In comparison to a standard of the injected solution, results were expressed as a percentage of the injected dose (%ID) per organ and per gram of each organ or tissue. For total blood radioactivity calculation, blood was assumed to be 7% of the total body weight. Radiolabeled FeHA NPs *ex vivo* behavior was studied at one mouse per time point for two main reasons: i) to contribute to the 3Rs' principles, by minimizing the number of animals, and to be used as a validation tool to the quantification imaging studies that enable the repetitive *in vivo* monitoring to 24 h post-injection.

Imaging studies were performed on a dedicated benchtop mouse-sized gamma camera (γ-eye by BET Solutions, Athens, Greece) [41], in combination with the X-ray part of a custom-made tri-modal system [42]. The gamma camera was based on two position-sensitive photomultiplier tubes, coupled to a CsI(Na) pixelated scintillator and a low-energy lead collimator with parallel hexagonal holes. The system's field of view was 5x10 cm^2, with spatial resolutions of 2 mm and energy resolution of ~25%. The x-ray system consisted of an x-ray tube and a CMOS detector, separated by a distance of 30 cm. The minimum pixel size is equal to 0.1 mm and the active area is approximately 12 ×12 cm.

For the scintigraphy imaging studies 100 μL ~0.01mCi (0.37 MBq) corresponding to ~400 μg of radiolabeled FeHA (0.3 mg Fe per body mouse) were administered through the tail-vein prior to anesthesia in normal mice. Anesthetization was performed intra-peritoneally with 100 μL 10 g^{-1} body weight of a stock solution containing 10% ketamine–hydrochloride (100 mg mL^{-1}), 5% xylazine–hydrochloride (20 mg mL^{-1}) prior to scanning. Then the mice were positioned on the animal bed at a <0.5 cm distance from the camera head to allow whole body imaging with maximum spatial resolution and successive 2 min frames were collected for up to 1 h post injection. After the first hour, static images were also acquired at 2, 4 and 24 h post injection. ROIs were drawn on major organs of interest and then these ROIs were applied to the individual frames, to provide semi-quantitative time activity curves. The ratio of counts in a ROI over the total number of counts was proportional to the radioactivity percentage per organ. Upon completion of the scintigraphy imaging, x-ray images were also acquired at the exact same mouse positioning to act as an anatomical guide for the organs exact location. The x-ray imaging parameters were set to 35 kVp, 500 μA and 0.1 s exposure time. Fusion

between scintigraphy and x-ray images was performed semi-automatically through an in-house standard procedure.

3. Results and Discussion

3.1 Nanoparticles Physicochemical Characterization

In **Fig. 1a** and in **Fig. 1b,** representative TEM micrographs of Endorem® and FeHA are respectively reported. Endorem® is made of very small (< 5 nm) round shaped electron dense NPs, while FeHA NPs consist of (i) small isometric crystals of about 5–10 nm aggregated in needle-like NPs having a length of 70-100 nm and width of 15-20 nm, and (ii) "dark spots" on the surface of needle-like ones corresponding to round-shaped electron dense NPs with a diameter in the 5-15 nm size range. As previously reported, these "dark spots" are maghemite NPs whose formation as secondary phase is due to the combination of two mechanisms occurring during FeHA synthesis: (i) Fe^{2+} oxidation, and (ii) oxidation of magnetite formed by co-precipitation [24].

FeHA and Endorem® in HEPES buffer at pH 7.4 have negative zeta potential of -44.1 ± 0.9 mV and -25.0 ± 0.2 mV respectively, and the relative hydrodynamic diameter (H_d) size-distributions at NPs concentrations corresponding to 1 mg/mL of Fe determined by DLS are markedly overlapped as shown in **Fig. 1c**. More in detail, the H_d size distribution recorded for FeHA shows NPs with a zeta-average of 179.1 ± 3.2 nm, while Endorem® features a zeta-average of 105.2 ± 2.0 nm. Both these size values are sensibly higher respect to that found by TEM due to the formation of NPs aggregates. A high degree of poly-dispersity (PDI = 0.35) due to the presence of relevant aggregates within the dextran matrix has been measured for Endorem®, in agreement with a previous work on Ferumoxide [33]. FeHA showed a more narrowed H_d distribution and a lower PDI of 0.20. Finally, it can be stated that the primary particles of Endorem® are much smaller respect to FeHA NPs, as determined by TEM in dry state, but they form agglomerates with comparable sizes and similar zeta potentials when suspended in a buffer at physiological pH. It is worth noticing that DLS measurements were carried out on FeHA and Endorem® suspensions at different NPs concentrations, namely 10.3 mg mL^{-1} and 1.43 mg mL^{-1} respectively, to keep constant the iron concentration.

XRD pattern of FeHA reported in **Fig. S1a** features broad and poorly defined peaks typical of bone nanocrystalline apatite, that can be indexed according to the crystallographic features of HA (JCPDS no. 09-432) [17, 43]. The presence of the peak at 35.4° corresponding to (311) plane of Fe_3O_4 (JCPDS no. 00-004-0755) established the presence of a small amount of maghemite that was estimated by Rietveld refinement to account for the 5.5 ± 0.7 wt% corresponding to about the 4.0 wt % of iron in FeHA, as already reported in previous works [23, 24]. By subtracting this amount to the total iron

content, the quantity of iron inside the crystal structure was the 5.7 wt%. **Tab.1** summarizes both FeHA and Endorem® chemical composition highlighting that the total content of iron of FeHA was notably lower than that of Endorem®. TGA analysis revealed a limited amount of carbonate derived from the atmospheric CO_2 that was adsorbed on the surface or entrapped in the crystal lattice during the synthesis, in agreement with previous reports [16, 23, 24].

Table 1 FeHA and Endorem® composition.

		Iron Oxide		Hydroxyapatite					
Sample	Fe(tot)[a]	Phase	Fe[b]	Fe[a]	Ca[a]	P[a]	Carbonate[c]	Ca/P[a]	Ca+Fe/P[a]
	(wt%)	(wt%)[b]	(wt%)	(wt%)	(wt%)	(wt%)	(wt%)	mol	mol
FeHA	9.7±0.4	5.5±0.7	4.0±0.5	5.7±0.5	28.8±1.2	14.9±1.0	1.8±0.5	1.49±0.07	1.70±0.07
Endorem®	71.1±2.2	-	-	-	-	-	-		

[a] Determined from ICP analysis
[b] Determined by Rietveld refinement of XRD pattern
[c] Determined by TGA analysis

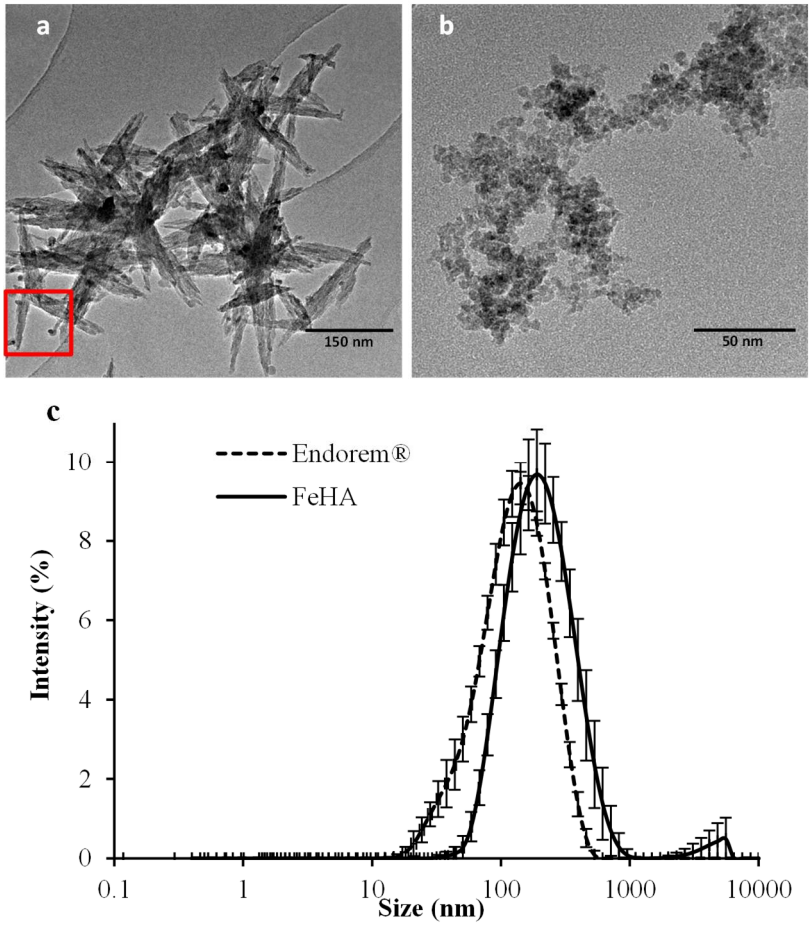

Fig.1 TEM micrographs of FeHA (a) and Endorem® NPs (b). The red box in panel (a) highlights the presence of small (10 nm) round shapes maghemite NPs on the surface of needle-like FeHA NPs. Size istribution of the hydrodynamic diameter of the two NPs (c) in an HEPS buffer at pH = 7.4.

The effective substitution of iron for calcium was proved by the Ca/P ratio that is lower compared to stoichiometric HA (i.e. 1.67), and by the (Ca+Fe)/P ratio which is very close to the value of 1.67 indicating a one to one Ca replacement with Fe. In this regard, we reported in a previous work that the one to one substitution of Ca^{2+} ion with $Fe^{2+/3+}$ ions prompts the arising of its superparamagnetic behavior [44].

The hysteresis loop, zero-field cool (ZFC) and field-cool (FC) collected on FeHA NPs and reported in **Fig. S2B**, **S2C** and **S2D** respectively are typical of superparamagnetic NPs with mass magnetization at saturation (M_s) of 8.7 emu g^{-1} after subtraction of the paramagnetic contribution. The mechanisms occurring at the nano/atomic scale and determining the unusual magnetic behavior of FeHA, which exhibits a very high net magnetic moment per iron atoms equal to 130 emu g^{-1} of Fe, were described in details elsewhere [24].

3.2 ^{1}H-NMR dispersion (NMR-D) profiles and relaxivity properties

Fig. 2a-b show the ^{1}H-NMR dispersion (^{1}H-NMRD) profiles of FeHA and Endorem® which were collected in the same range of frequency used by most common clinical imaging devices operating at 0.2, 0.5, and 1.5 Tesla corresponding to ~ 8, 20, and 64 MHz. The collection of ^{1}H-NMR dispersion profiles in such a wide frequency range was motivated by the need to investigate the mechanisms responsible for nuclear relaxation through the analysis of the frequency behavior (profile) of FeHA longitudinal (r_1), and transverse (r_2) nuclear relaxivities.

To obtain ^{1}H-NMRD profiles, the nuclear relaxivities r_1 and r_2, defined by the following equation as:

$$r_i = [(1/T_i)_{meas} - (1/T_i)_{dia}]/c \qquad i = 1,2 \qquad (1)$$

where $(1/T_i)_{meas}$ is the value measured for the sample with concentration of magnetic centers c (Fe mmol L^{-1}) and $(1/T_i)_{dia}$ represents the nuclear relaxation rate of the diamagnetic host solution (citrate buffer 0.1 wt%).

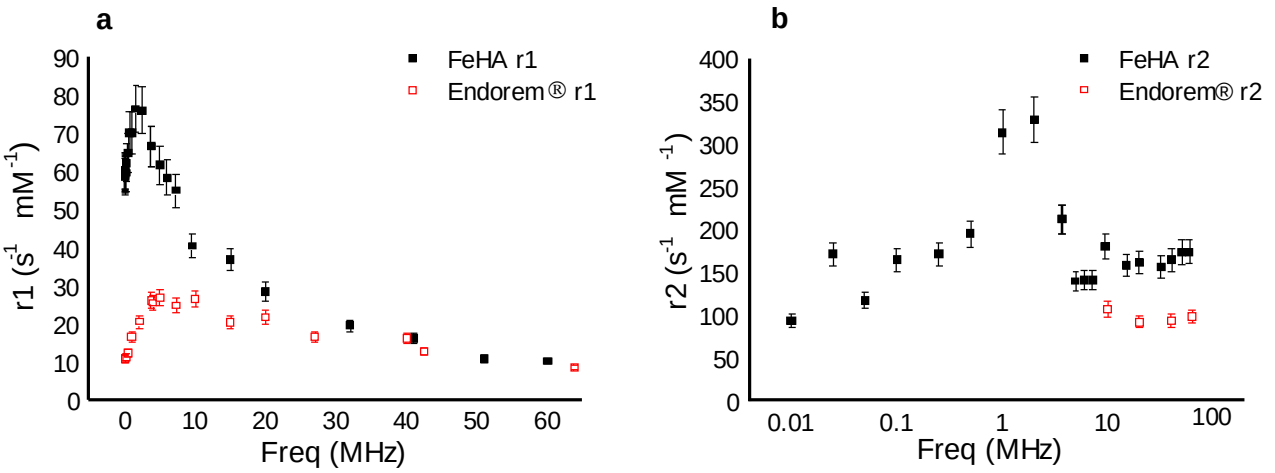

Figure 2 r1 (a) and r2 (b) ^{1}H-NMRD profiles of FeHA and Endorem® at equivalent iron concentration (Fe 0.2 mM) in a 0.1 wt% citrate buffer and measured at room temperature in the frequency range $0.01 < f < 100$ MHz.

The r_1 profiles of FeHA and Endorem® display similar shapes, typical of superparamagnetic NPs, with some differences due to the different sizes of the materials [45]. For example, the maximum peak position for Endorem® NPs is shifted towards higher frequencies with respect to FeHA consistently to the smaller magnetic domain size of Endorem®. On the other hand, the r_2 values measured at 0.2 Tesla (~ 8.5 MHz), which is a field intensity commonly used for orthopedic MRI investigation, were $r_2^{FeHA} \sim 165\ s^{-1}\,mM^{-1}$ and $r_2^{Endorem®} \sim 103\ s^{-1}\,mM^{-1}$. Indeed both r_1 and r_2 of FeHA are higher than Endorem®, thus suggesting that the former would led to a higher contrast in negative MRI images with respect to latter in this range of frequencies.

To investigate further the MRI ability of the two NPs, five Endorem® and five FeHA aqueous solutions at increasing Fe concentration - together with water as reference system - were analyzed by T_2-weighted MRI on a 7 Tesla (~ 300 MHz) preclinical magnetic resonance scanner. The images reported in **Fig. 3a** substantially confirm the efficiency of both NPs as T_2 weighted CA. **Fig. 3b** displays the relaxation rates $1/T_2$ of both FeHA and Endorem® as a function of Fe concentration showing the linear relation between the two parameters according to equation (1), where r_2 is the slope of the lines obtained by least square regression of the two sets of data.

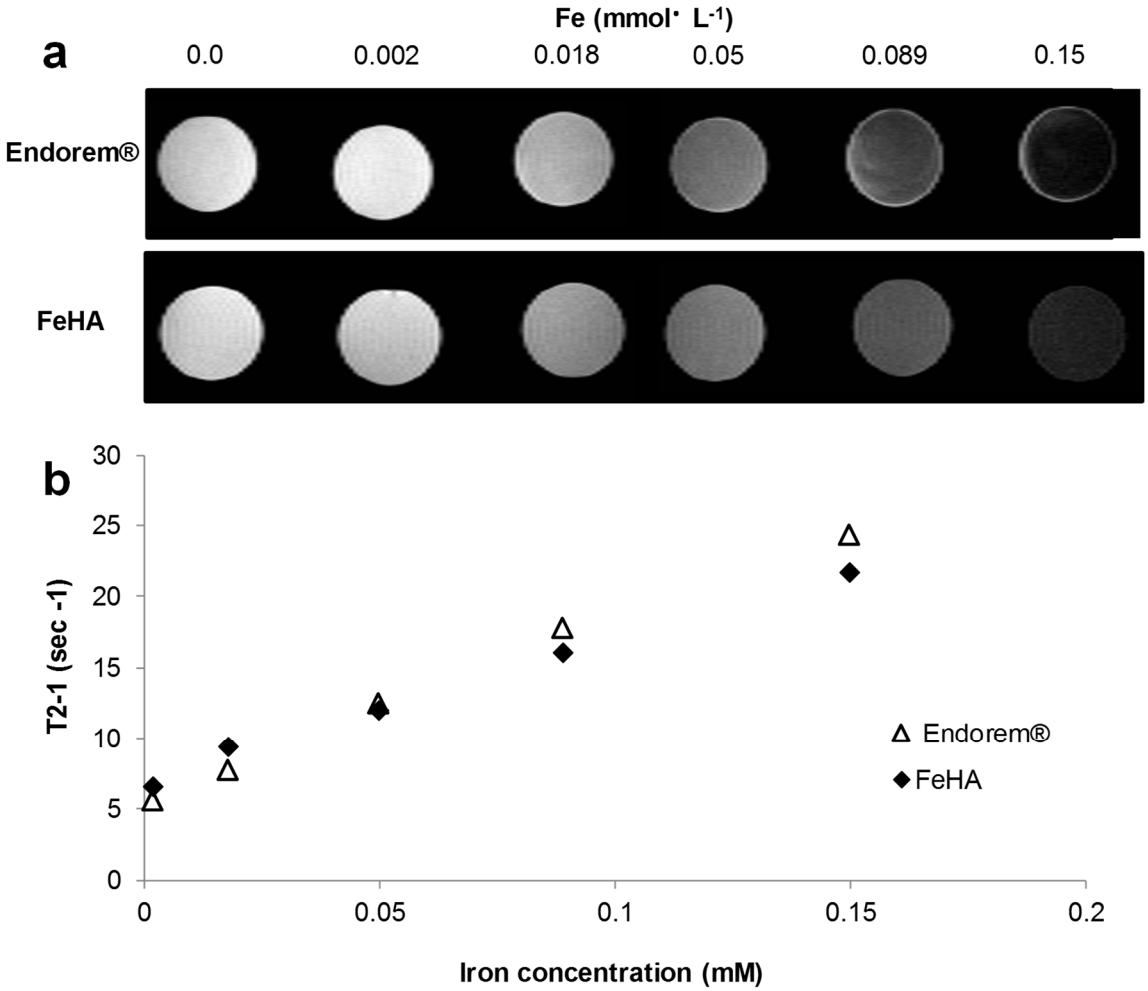

Figure 3. MRI images on FeHA and Endorem® at increasing Fe concentrations (a). The sequence used was a MSME. The relaxation rates $1/T_2$ of both FeHA and Endorem® are linearly related to the iron concentration in the solution (b). Values were measured from a ROI of 0.04 cm^2. Standard deviation is < 1%

The so estimated r_2 value for FeHA (99.2 mM^{-1} s^{-1}) is lower than that of Endorem® (127.7 mM^{-1} s^{-1}) which is very similar to those already reported in the literature for other Ferumoxide-based CAs (e.g. Feridex) [33]. These values are more similar to one another with respect to those found by ^{1}H-NMR, but substantially confirm the FeHA efficiency in enhancing the negative contrast in T_2 weighted MRI.

3.3 Preliminary *in vivo* measurements

The contrast abilities of Endorem® and FeHA were tested *in vivo* on healthy mice to compare their performances in an operational environment. For both NPs, the contrast enhancement achieved in the liver was measured at different time points. The choice of this target organ was motivated by the fact that liver imaging was the first clinical application of MNPs in the form of Ferumoxides (AMI-25, Endorem® and Feridex IV®) as documented by the wide literature reporting on these CAs [2, 27, 30-32, 46].

Mice were administered with 140 μL of both FeHA and Endorem® solutions to obtain an equivalent dose of 1 mg of Fe per kg of mouse as already reported by other works on SPION-based CAs [47, 48]. Images of the target organ were collected before the CA intravenous administration (basal), and then at 10 minutes and 24 hours post injection. The spleen and the renal cortex of treated mice were also examined to assess the distribution of the CAs in organs in which other cells of the MPS are located.

Table 2. *In vivo* T_2 relaxation times derived from MR images collected at different time points on two mice treated with an equivalent iron dose (1 mg kg^{-1}) of FeHA and Endorem®.

	Liver (msec)			**Spleen (msec)**			**Renal cortex (msec)**		
	Basal	**Post**	**24h**	**Basal**	**Post**	**24h**	**Basal**	**Post**	**24h**
Endorem®	25.5±1.2	21.0±1.8	25.8±1.1	33.3±1.3	33.6±1.6	32.6±0.5	46.9±3.1	42.9±2.3	46.2±2.9
FeHA	20.7±0.4	11.7±0.4	14.6±0.3	33.5±1.3	25.8±0.5	24.8±0.9	57.8±4.8	47.2±2.9	39.5±2.3

The relative T_2 relaxation times tabulated in **Table 2** and the MR images depicted in **Fig.4a-b** show that both Endorem® and FeHA determined a relevant enhancement of the liver contrast (student-t test, $p<0.05$) at 10 min post injection. This enhancement was much stronger and lasted for longer time (up to 24 hours) in the mice treated with FeHA than in the ones treated with Endorem®; in addition, while the administration of the latter did not sort any effect on the spleen and the renal cortex, FeHA NPs determined a marked secondary contrast enhancement on these organs up to 24 hours.

The quick normalization of the T_2 signals in the three organs of the mice treated with Endorem®, denotes that NPs were almost completely eliminated from the relative tissues after the first 24 hours. Such a rapid removal is likely to be due to their dissolution operated by lysosomes and favored by the quick removal of the dextran coating, as it is well known that these NPs are selectively up-taken by MPS macrophages and that their degradation is strictly dependent on the coating stability [8, 49, 50].

On the other hand, the contrast enhancing effect of FeHA on the liver started to decrease after 24 hours post injection while at the same time point, the contrast enhancements on the spleen and the renal cortex were higher respect to those achieved after 10 minutes.

As can be seen from the relative T_2 values reported in **Tab.2**, since FeHA NPs were found to persist in the three monitored organs above the first 24 hours we extended the follow up and collected MRI images on a daily base up to 10 days to monitor FeHA clearance/degradation. The graph reported in **Fig. 5** shows that the contrast enhancement effect produced by FeHA in the examined organs was lost only after 7 days, indicating that the clearance of the NPs from these areas was definitely slower respect to Endorem®.

The investigation of the *in vivo* biological transformations of the tested MNPs is beyond the scope of this study, but there is no reason to believe that FeHA NPs underwent through a different path with respect to that followed by Endorem® NPs consisting in their dissolution by lysosomes followed by iron bio-adsorption and incorporation into hemoglobin [47, 50, 51].

Bio-resorbability is a well-known property of nanocrystalline carbonated calcium phosphate, and since the persistence of FeHA NPs in the target organs is unlikely to be due to their higher resistance to biological degradation, the discrepancy with the clearance/degradation of Endorem® is fully ascribable to the higher quantity of injected FeHA (10.30 mg vs 1.43 mg). In fact, the rate of degradation of Ferumoxide in the liver Kupffer and endothelial cells was proved to be dependent upon the dose administered [33], complying with the lower endurance of Endorem® respect to FeHA observed in the present study. Moreover, we exclude that the differences observed in the liver clearance rates of FeHA and Endorem® are ascribable to their sizes as the two NPs displayed similar H_d distributions at physiological pH. In addition, the difference in primary particle sizes cannot sort any sensible effect on their clearance, but can only enhances the uptake by macrophage cells both *in vitro* and *in vivo* [8, 52-54].

In conclusion, the higher contrast enhancement in the liver, spleen and renal cortex obtained with FeHA than with Endorem® is due to the higher number of FeHA NPs injected and to the higher uptake by the MPS cells as the two materials display comparable r_2 at the field intensity and frequency used for the *in vivo* experiment.

It is important to take into account that, while for CAs based on Gd-chelates their rapid elimination from the body is crucial to minimize the time period for Gd chelates to decomplexate and exert subsequent toxicity [55], in the case of SPION based CAs the risk for patients health is represented by the accumulation of high loads of iron in the area of interest. In fact, the clearance mechanisms of SPIONs and Gd-chelates are very different as Gd based CA goes through a rapid renal clearance – though its accumulation in bones and brain has been documented by some studies [56] - while SPIONs based CA usually have longer persistence in the body. Moreover, SPIONs diagnostic potential depends on its concentration in the diagnostic organ/tissue thus requiring the targeting of NPs to a specific site and determining the accumulation of high amounts of iron in the treatment area. Eventually, the rapid dissolution of these NPs can cause the burst release of high quantities of Fe ions in the exposed tissue, leading to cytotoxicity, DNA damage and other mechanisms responsible of iron-induced carcinogenesis [8, 11, 12, 57]. At this regard, it is worth to remark that FeHA NPs have a lower Fe content with respect to Endorem® and that, in this experiment, the iron dose administered to each mouse was calibrated to reach an equal dose of iron (1 mg kg^{-1}) for both the CAs in the mice body.

The higher contrast ability displayed by FeHA with respect to Endorem® opens to the possibility of reducing the iron amounts in the body having at the same time an equivalent contrast enhancements and less risks for the health of patients.

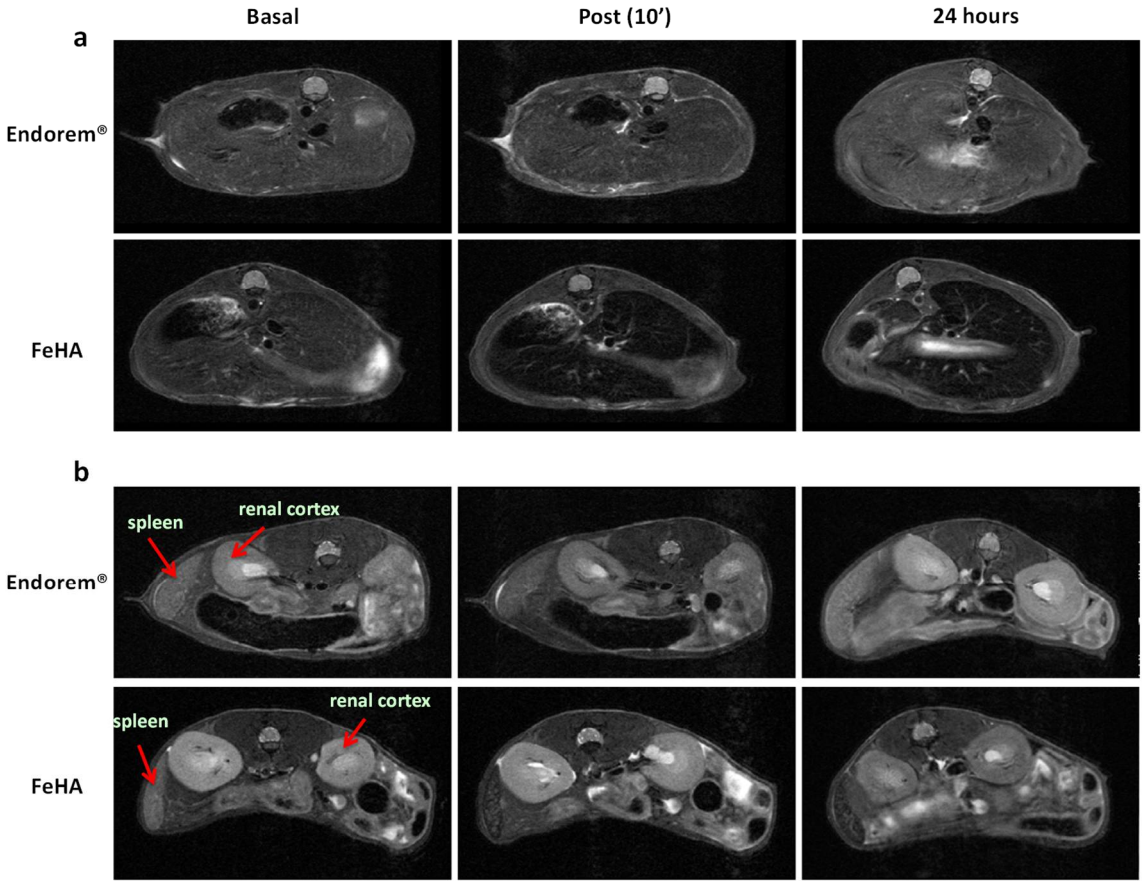

Fig. 4 *In vivo* RARE T2-weighted sequence, MRI images of liver (a), spleen and renal cortex (b) collected at different time points after intravenous administration of FeHA and Endorem® at a dose of 1.0 mg kg^{-1}.

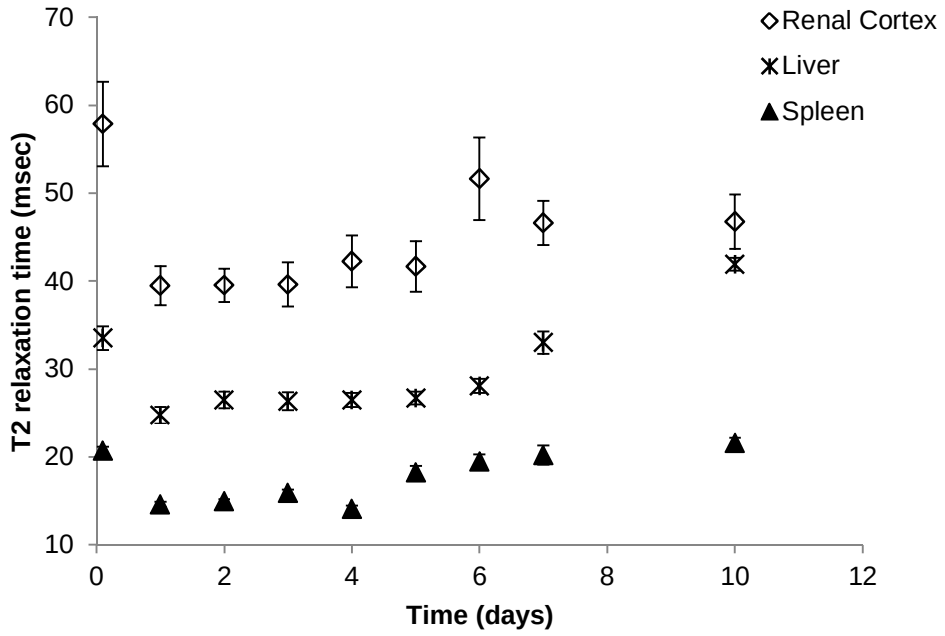

Fig. 5 *In vivo* T_2 relaxation times (MSME) from MRI images of renal cortex, spleen and liver at different time points after intravenous administration of a dose of FeHA corresponding to 1.0 mg of iron per kg of animal.

3.4 Radiolabeling of FeHA

Radiolabeling of FeHA with ^{99m}Tc was obtained by simply mixing ^{99m}Tc-MDP solutions with a suspension of FeHA NPs. The chemical affinity of the MDP for HA due to the strong chemical binding of the bisphosphonate arm with the surface calcium sites of bone and synthetic HA is well reported [58, 59]. In fact, bisphosphonates tagged radionuclides, including ^{99m}Tc-MDP, are routinely used in bone scintigraphy applications for the diagnosis of bone metastasis, inflammation, fractures and infection, while radionuclide conjugated HA microparticles are used in clinics for therapeutic applications such as radiation synovectomy[59].

^{99m}Tc has been selected because it is considered as the most suitable radioisotope for nuclear imaging due to its availability, simple conjugation chemistry, short half-life of 6 h and 140 keV gamma emission which is ideal for the existing Auger cameras [60].

The two-strip ITLC-SG method for the analysis of ^{99m}Tc-MDP showed that post labeling no amount of either pertechnetate ($^{99m}TcO_4^-$) or of colloidal ^{99m}Tc ($^{99m}TcO_2$) was present, as shown in **Fig. S2a-c**, respectively. The radiochemical yield for ^{99m}Tc-MDP-FeHA was 65.9 ± 4.7 % providing a single radioactive species, as detected by paper chromatography (Whatman 3MM) reported in **Fig. S2c**.

Kinetic stability studies up to 24 h of the radiolabeled FeHA NPs at different temperatures and in different media at 37°C are reported in **Fig. 6** showing that the labeling was stable. More in detail, in water solution at different temperatures and in isotonic saline solution more than 90 % of the radioactivity was found in the NPs up to 24 hours, while a partial radiolabel loss in fetal bovine and in human serum of 25% and 40% respectively was observed after 24 hours. This behavior could be attributed to the fact that radiolabeled FeHA NPs were recognized by serum proteins which dispose high affinity for iron, thus determining the partial decoupling of ^{99m}Tc-MDP from NPs.

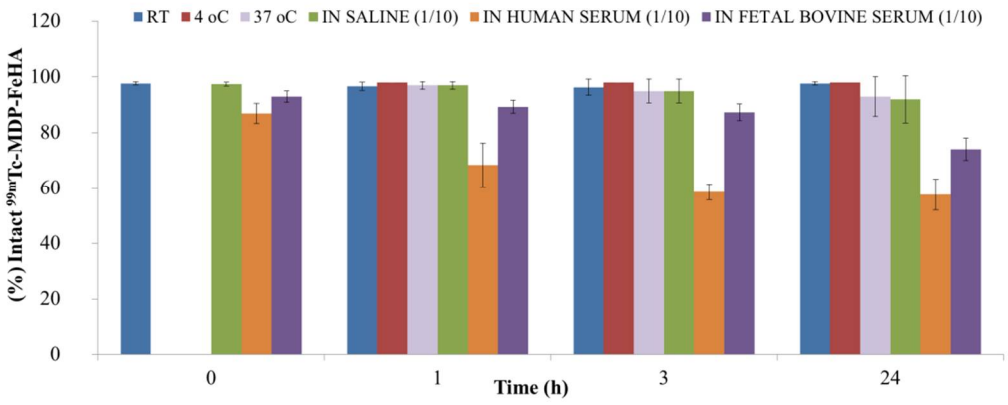

Figure 6. *In vitro* stability of ^{99m}Tc-MDP-FeHA at various time points post preparation incubated in water at three different temperatures (room temperature, 4°C and 37°C) and in different media (isotonic saline solution, human and fetal bovine serum) at room temperature.

3.5 Biodistribution and whole body scintigraphy/x-ray fused imaging

Ex vivo studies in healthy Swiss mouse models at 30 min, 40 min, 4 h and 24 h post injection for ^{99m}Tc-MDP-FeHA are summarized in **Fig. 7**. No significant uptake or retention was observed neither in the stomach (data not shown) nor in the thyroid gland (imaging study), indicating that there was minimal, if any, free $^{99m}TcO_4^-$. Liver activity values were significantly high for all the tested time points. A detectable spleen uptake was noticed from 30 min up to 24 h post injection. The radioactivity detected in bones after 24 hours could be due to the initial degradation of FeHA into the liver causing the partial loss of the radioligand from the NPs.

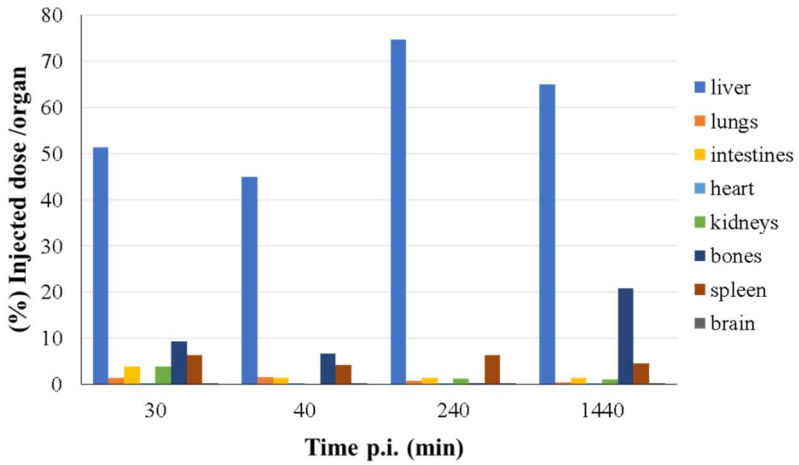

Figure 7 *Ex vivo* tissue biodistribution of radioactivity at 30 min, 40 min, 4 h and 24 h post injection of the ^{99m}Tc-MDP-FeHA (0.3 mg iron per kg of animal and 0.37 MBq).

Scintigraphic imaging studies on anesthetized healthy Swiss mice were performed on a dedicated small animal scintigraphic/x-ray system, up to 1 h, and at 2 and 24 h post injection as depicted in **Fig. 8**.

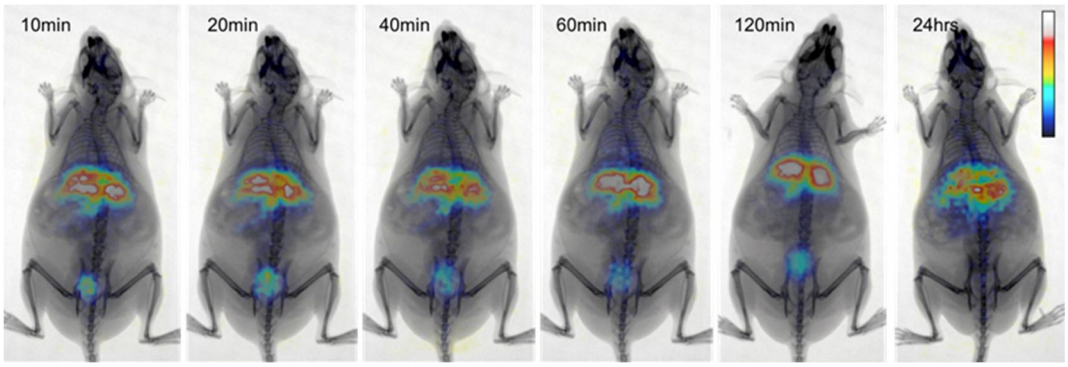

Figure 8 Static 2 min scintigraphy/X-ray images of healthy Swiss Albino mice collected at different time points after intravenous administration of radiolabeled FeHA NPs.

The biodistribution of FeHA NPs as determined by the analysis of scintigraphy images (**Fig. S3** and dynamic imaging of the first 38 minutes post injection reported in the supplementary information**)** is in good agreement with that determined by *ex vivo* analysis. Liver was found to be the dominant accumulation organ at all the time points, although the concentration of radiolabeled FeHA in other organs of MPS (like spleen and bone marrow) was not negligible. These results are in good agreement with a previous report on Endorem® radiolabeled with ^{99m}Tc-Bisphosphonate in which the authors found accumulation in liver and spleen [61]. However, comparing the feature of Endorem® and FeHA as nuclear imaging agents, the main difference is that Endorem® NPs had to be heated up to 100°C to partially remove the dextran coating to allow an effective conjugation between radioligand molecules and the NPs surface. Conversely, as already well reported for iron-free HA NPs [62], FeHA can be conjugated with bisphosphonates tagged radionuclides by a simple one-pot procedure carried out at room temperature.

Conclusions

In the last decade, clinical concerns associated with the use of SPIONs have emerged due to the accumulation of high iron loads associated to their use in localized areas of the body. Here, we reported on the performance as MRI contrast agent for the liver, the spleen and the renal cortex of intrinsically biocompatible FeHA NPs.

A suspension of FeHA was injected intravenously *in vivo* in mice at a low iron dose (1 mg kg^{-1}) and was found (i) to apply a higher contrast enhancement, and (ii) to have a longer endurance in the liver with respect to Endorem® at iron equality. These phenomena were related respectively to the high transversal relaxation rate and to the higher quantity of FeHA NPs that were administered respect to Endorem® to reach the same iron dose, as the two materials display different amounts of iron (9.7 wt% vs 71.0 wt%). Moreover, FeHA NPs were found to enhance the negative contrast also in spleen and renal cortex tissues, while on the contrary Endorem® was detected in significant concentration only in the liver.

A straightforward labelling methodology involving a surface functionalization with ^{99m}Tc-MDP was successfully applied on FeHA NPs to potentially extend their application as multimodal MRI/PET-SPECT imaging agents. In fact, the combination of imaging techniques such as nuclear and magnetic can improve the diagnostic ability taking the advantages of each technique such as deep tissue penetration of radiation signals, anatomical and functional details provided by magnetic contrast. The collected imaging and biodistribution results by scintigraphy/x-ray fused imaging and *ex vivo* studies

confirmed the dominant accumulation of FeHA NPs in the liver, and secondarily in other MPS organs, as detected by MRI.

Although further *in vitro* and *in vivo* studies on FeHA long-term cytotoxicity are necessary especially on Kupffer cells and on other cells of the MPS as well as the *in vivo* validation of SPECT-MRI detection, its performance as contrast agent for MRI-T_2 and PET-SPECT combined to its ability to work as nanocarrier for bioactive molecules as previously reported (Citation) qualifies FeHA as one of the most resourceful nanomaterial for the design of new theranostic agents for interesting personalized medical applications.

Akcnowledgments

The authors acknowledge the European Community for its financial support in the framework of the project CUPIDO (www.cupidoproject.eu) H2020-NMBP-2016 720834. The authors also thank Dr. Raffaella Rizzo for her comments on kidneys clearance.

References

1. Neuberger, T., et al., *Superparamagnetic nanoparticles for biomedical applications: possibilities and limitations of a new drug delivery system.* Journal of Magnetism and Magnetic Materials, 2005. **293**(1): p. 483-496.
2. Jain, T.K., et al., *Magnetic nanoparticles with dual functional properties: drug delivery and magnetic resonance imaging.* Biomaterials, 2008. **29**(29): p. 4012-21.
3. Majewski, A.P., et al., *Dual-responsive magnetic core–shell nanoparticles for nonviral gene delivery and cell separation.* Biomacromolecules, 2012. **13**(3): p. 857-866.
4. Iannotti, V., et al., *Magnetic anisotropy in Ni–Si nanoparticle films produced by ultrashort pulsed laser deposition.* Journal of Magnetism and Magnetic Materials, 2008. **320**(20): p. e594-e598.
5. Liu, G., et al., *Applications and potential toxicity of magnetic iron oxide nanoparticles.* Small, 2013. **9**(9-10): p. 1533-45.
6. Ling, D. and T. Hyeon, *Iron Oxide Nanoparticles: Chemical Design of Biocompatible Iron Oxide Nanoparticles for Medical Applications (Small 9–10/2013).* Small, 2013. **9**(9-10): p. 1449-1449.
7. Bixner, O., et al., *Complete Exchange of the Hydrophobic Dispersant Shell on Monodisperse Superparamagnetic Iron Oxide Nanoparticles.* Langmuir, 2015. **31**(33): p. 9198-204.
8. Huang, J., et al., *Effects of nanoparticle size on cellular uptake and liver MRI with polyvinylpyrrolidone-coated iron oxide nanoparticles.* ACS nano, 2010. **4**(12): p. 7151-7160.
9. Dai, L., et al., *One-pot facile synthesis of PEGylated superparamagnetic iron oxide nanoparticles for MRI contrast enhancement.* Mater Sci Eng C Mater Biol Appl, 2014. **41**: p. 161-7.
10. Wang, Y.X., *Superparamagnetic iron oxide based MRI contrast agents: Current status of clinical application.* Quant Imaging Med Surg, 2011. **1**(1): p. 35-40.
11. Lunov, O., et al., *Lysosomal degradation of the carboxydextran shell of coated superparamagnetic iron oxide nanoparticles and the fate of professional phagocytes.* Biomaterials, 2010. **31**(34): p. 9015-22.
12. Singh, N., et al., *Potential toxicity of superparamagnetic iron oxide nanoparticles (SPION).* Nano Rev, 2010. **1**.
13. Wei, Y., et al., *Iron overload by superparamagnetic iron oxide nanoparticles is a high risk factor in cirrhosis by a systems toxicology assessment.* Scientific reports, 2016. **6**: p. 29110.
14. Borm, P.J., et al., *The potential risks of nanomaterials: a review carried out for ECETOC.* Particle and fibre toxicology, 2006. **3**(1): p. 11.
15. Gómez-Morales, J., et al., *Progress on the preparation of nanocrystalline apatites and surface characterization: overview of fundamental and applied aspects.* Progress in Crystal Growth and Characterization of Materials, 2013. **59**(1): p. 1-46.
16. Iafisco, M., et al., *Superparamagnetic iron-doped nanocrystalline apatite as a delivery system for doxorubicin.* Journal of Materials Chemistry B, 2016. **4**(1): p. 57-70.
17. Panseri, S., et al., *Magnetic Labelling of Mesenchymal Stem Cells with Iron-Doped Hydroxyapatite Nanoparticles as Tool for Cell Therapy.* Journal of Biomedical Nanotechnology, 2016. **12**(5): p. 909-921.

18. Tesch, A., et al., *Luminomagnetic Eu3+-and Dy3+-doped hydroxyapatite for multimodal imaging.* Materials Science and Engineering: C, 2017. **81**: p. 422-431.
19. Oliveira, E., A. Rossi, and R. Santos-Oliveira, *Nano-Hydroxyapatite Doped with Ho-166 as Drug Delivery System for Bone Cancer Therapy and Diagnosis: Developing a Theragnostic Radiopharmaceuticals.* Anti-cancer agents in medicinal chemistry, 2017. **17**(3): p. 355-358.
20. Zhao, R., et al., *Selective effect of hydroxyapatite nanoparticles on osteoporotic and healthy bone formation correlates with intracellular calcium homeostasis regulation.* Acta biomaterialia, 2017. **59**: p. 338-350.
21. Chen, F., et al., *The photoluminescence, drug delivery and imaging properties of multifunctional Eu 3+/Gd 3+ dual-doped hydroxyapatite nanorods.* Biomaterials, 2011. **32**(34): p. 9031-9039.
22. Muñoz Úbeda, M., et al., *Gadolinium-Decorated Silica Microspheres as Redox-Responsive MRI Probes for Applications in Cell Therapy Follow-Up.* Chemistry-A European Journal, 2016. **22**(23): p. 7716-7720.
23. Tampieri, A., et al., *Intrinsic magnetism and hyperthermia in bioactive Fe-doped hydroxyapatite.* Acta biomaterialia, 2012. **8**(2): p. 843-851.
24. Iannotti, V., et al., *Fe-Doping-Induced Magnetism in Nano-Hydroxyapatites.* Inorganic Chemistry, 2017. **56**(8): p. 4446-4458.
25. Liu, Y., et al., *Long-term biodistribution in vivo and toxicity of radioactive/magnetic hydroxyapatite nanorods.* Biomaterials, 2014. **35**(10): p. 3348-3355.
26. Xu, Y.-J., et al., *Magnetic hydroxyapatite nanoworms for magnetic resonance diagnosis of acute hepatic injury.* Nanoscale, 2016. **8**(3): p. 1684-1690.
27. Singh, A. and S.K. Sahoo, *Magnetic nanoparticles: a novel platform for cancer theranostics.* Drug Discovery Today, 2014. **19**(4): p. 474-481.
28. Jordan, A., et al., *Presentation of a new magnetic field therapy system for the treatment of human solid tumors with magnetic fluid hyperthermia.* Journal of magnetism and magnetic materials, 2001. **225**(1): p. 118-126.
29. Andreas, K., et al., *Highly efficient magnetic stem cell labeling with citrate-coated superparamagnetic iron oxide nanoparticles for MRI tracking.* Biomaterials, 2012. **33**(18): p. 4515-4525.
30. Saini, S., et al., *Ferrite particles: a superparamagnetic MR contrast agent for the reticuloendothelial system.* Radiology, 1987. **162**(1): p. 211-216.
31. Reimer, P., et al., *T1 effects of a bolus-injectable superparamagnetic iron oxide, SH U 555 A: dependence on field strength and plasma concentration--preliminary clinical experience with dynamic T1-weighted MR imaging.* Radiology, 1998. **209**(3): p. 831-836.
32. Ba-Ssalamah, A., et al., *Detection of focal hepatic lesions: Comparison of unenhanced and SHU 555 A-enhanced MR imaging versus biphasic helical CTAP.* Journal of Magnetic Resonance Imaging, 2000. **11**(6): p. 665-672.
33. Briley-Saebo, K.C., et al., *Clearance of iron oxide particles in rat liver: effect of hydrated particle size and coating material on liver metabolism.* Investigative radiology, 2006. **41**(7): p. 560-571.
34. Pichler, B.J., et al., *PET/MRI: paving the way for the next generation of clinical multimodality imaging applications.* Journal of Nuclear Medicine, 2010. **51**(3): p. 333-336.
35. Thorek, D.L., et al., *Non-invasive mapping of deep-tissue lymph nodes in live animals using a multimodal PET/MRI nanoparticle.* Nature communications, 2014. **5**: p. 3097.
36. Brodsky, E.K., et al., *High-spatial and high-temporal resolution dynamic contrast-enhanced perfusion imaging of the liver with time-resolved three-dimensional radial MRI.* Magnetic resonance in medicine, 2014. **71**(3): p. 934-941.
37. Lahooti, A., et al., *PEGylated superparamagnetic iron oxide nanoparticles labeled with 68Ga as a PET/MRI contrast agent: a biodistribution study.* Journal of Radioanalytical and Nuclear Chemistry, 2017. **311**(1): p. 769-774.

38. Kolosnjaj-Tabi, J. and C. Wilhelm, *Magnetic nanoparticles in cancer therapy: how can thermal approaches help?* 2017, Future Medicine.
39. Iafisco, M., et al., *The cooperative effect of size and crystallinity degree on the resorption of biomimetic hydroxyapatite for soft tissue augmentation.* International Journal of Artificial Organs, 2010. **33**(11): p. 765-774.
40. Adamiano, A., et al., *Analytical pyrolysis-based study on intra-skeletal organic matrices from Mediterranean corals.* Analytical and bioanalytical chemistry, 2014. **406**(24): p. 6021-6033.
41. Georgiou, M., et al., *Characterization of "gamma-Eye": a Low-Cost Benchtop Mouse-Sized Gamma Camera for Dynamic and Static Imaging Studies.* Mol Imaging Biol, 2017. **19**(3): p. 398-407.
42. Rouchota, M., et al., *A prototype PET/SPECT/X-rays scanner dedicated for whole body small animal studies.* Hell J Nucl Med, 2017. **20**(2): p. 146-153.
43. Iafisco, M., et al., *Biomimetic magnesium–carbonate-apatite nanocrystals endowed with strontium ions as anti-osteoporotic trigger.* Materials Science and Engineering: C, 2014. **35**: p. 212-219.
44. Panseri, S., et al., *Intrinsically superparamagnetic Fe-hydroxyapatite nanoparticles positively influence osteoblast-like cell behaviour.* Journal of nanobiotechnology, 2012. **10**(1): p. 32.
45. Na, H.B., I.C. Song, and T. Hyeon, *Inorganic nanoparticles for MRI contrast agents.* Advanced materials, 2009. **21**(21): p. 2133-2148.
46. Clement, O., et al., *Contrast agents in magnetic resonance imaging of the liver: present and future.* Biomedicine & pharmacotherapy, 1998. **52**(2): p. 51-58.
47. Kreft, B., et al., *Diagnostic value of a superparamagnetic iron oxide in MR imaging of chronic liver disease in an animal model.* AJR. American journal of roentgenology, 1998. **170**(3): p. 661-668.
48. Turetschek, K., et al., *MR Imaging Characterization of Microvessels in Experimental Breast Tumors by Using a Particulate Contrast Agent with Histopathologic Correlation 1.* Radiology, 2001. **218**(2): p. 562-569.
49. Arbab, A.S., et al., *A model of lysosomal metabolism of dextran coated superparamagnetic iron oxide (SPIO) nanoparticles: implications for cellular magnetic resonance imaging.* NMR in Biomedicine, 2005. **18**(6): p. 383-389.
50. Weissleder, R., et al., *Superparamagnetic iron oxide: pharmacokinetics and toxicity.* American Journal of Roentgenology, 1989. **152**(1): p. 167-173.
51. Kolosnjaj-Tabi, J., et al., *Biotransformations of magnetic nanoparticles in the body.* Nano Today, 2016. **11**(3): p. 280-284.
52. He, C., et al., *Effects of particle size and surface charge on cellular uptake and biodistribution of polymeric nanoparticles.* Biomaterials, 2010. **31**(13): p. 3657-3666.
53. Roca, A.G., et al., *Effect of nanoparticle and aggregate size on the relaxometric properties of MR contrast agents based on high quality magnetite nanoparticles.* The Journal of Physical Chemistry B, 2009. **113**(19): p. 7033-7039.
54. Koenig, S.H. and K.E. Kellar, *Theory of 1/T1 and 1/T2 NMRD profiles of solutions of magnetic nanoparticles.* Magnetic resonance in medicine, 1995. **34**(2): p. 227-233.
55. Ersoy, H. and F.J. Rybicki, *Biochemical safety profiles of gadolinium-based extracellular contrast agents and nephrogenic systemic fibrosis.* J Magn Reson Imaging, 2007. **26**(5): p. 1190-7.
56. Thakral, C., J. Alhariri, and J.L. Abraham, *Long-term retention of gadolinium in tissues from nephrogenic systemic fibrosis patient after multiple gadolinium-enhanced MRI scans: case report and implications.* Contrast media & molecular imaging, 2007. **2**(4): p. 199-205.
57. Ferrucci, J. and D. Stark, *Iron oxide-enhanced MR imaging of the liver and spleen: review of the first 5 years.* AJR. American journal of roentgenology, 1990. **155**(5): p. 943-950.

58. Ashokan, A., et al., *Multifunctional calcium phosphate nano-contrast agent for combined nuclear, magnetic and near-infrared in vivo imaging.* Biomaterials, 2013. **34**(29): p. 7143-7157.
59. Al-Bulushi, N.K. and M.-E. Abouzied, *Comparison of 18F-FDG PET/CT scan and 99mTc-MDP bone scintigraphy in detecting bone metastasis in head and neck tumors.* Nuclear medicine communications, 2016. **37**(6): p. 583-588.
60. Schipper, M.L., et al., *Efficacy of 99mTc pertechnetate and 131I radioisotope therapy in sodium/iodide symporter (NIS)-expressing neuroendocrine tumors in vivo.* European journal of nuclear medicine and molecular imaging, 2007. **34**(5): p. 638-650.
61. Torres Martin de Rosales, R., et al., *99mTc-bisphosphonate-iron oxide nanoparticle conjugates for dual-modality biomedical imaging.* Bioconjugate chemistry, 2011. **22**(3): p. 455-465.
62. Sandhofer, B., et al., *Synthesis and preliminary in vivo evaluation of well-dispersed biomimetic nanocrystalline apatites labeled with positron emission tomographic imaging agents.* ACS Appl Mater Interfaces, 2015. **7**(19): p. 10623-33.